



Pergamon

Available online at www.sciencedirect.com

SCIENCE @ DIRECT®

International Journal of Machine Tools & Manufacture 43 (2003) 1319–1326

INTERNATIONAL JOURNAL OF
**MACHINE TOOLS
& MANUFACTURE**
DESIGN, RESEARCH AND APPLICATION

Finite element modeling of friction stir welding—thermal and thermomechanical analysis

C.M. Chen, R. Kovacevic *

Research Center for Advanced Manufacturing, Department of Mechanical Engineering, Southern Methodist University, International Parkway, Suite 100, Richardson, TX 75081, USA

Received 12 May 2003; accepted 10 June 2003

Abstract

Friction stir welding (FSW) is a relatively new welding process that may have significant advantages compared to the fusion processes as follow: joining of conventionally non-fusion weldable alloys, reduced distortion and improved mechanical properties of weldable alloys joints due to the pure solid-state joining of metals. In this paper, a three-dimensional model based on finite element analysis is used to study the thermal history and thermomechanical process in the butt-welding of aluminum alloy 6061-T6. The model incorporates the mechanical reaction of the tool and thermomechanical process of the welded material. The heat source incorporated in the model involves the friction between the material and the probe and the shoulder. In order to provide a quantitative framework for understanding the dynamics of the FSW thermomechanical process, the thermal history and the evolution of longitudinal, lateral, and through-thickness stress in the friction stirred weld are simulated numerically. The X-ray diffraction (XRD) technique is used to measure the residual stress of the welded plate, and the measured results are used to validate the efficiency of the proposed model. The relationship between the calculated residual stresses of the weld and the process parameters such as tool traverse speed is presented. It is anticipated that the model can be extended to optimize the FSW process in order to minimize the residual stress of the weld.

© 2003 Elsevier Ltd. All rights reserved.

Keywords: Friction stir welding; Finite element method; Thermal history; Thermomechanical process; Evolutionary Stress; Residual stress

1. Introduction

Friction stir welding (FSW) is a recently emerged solid-state joining technology patented by The Welding Institute (TWI) in 1991 [1]. The process is illustrated in Fig. 1, where a rotating cylindrical shouldered tool plunges into the butted plates and locally plasticizes the joint region during its movement along the joint line that causes a joint between the work pieces. In this process, the heat is originally derived from the friction between the welding tool (including the shoulder and the probe) and the welded material, which causes the welded material to soften at a temperature less than its melting point. The softened material underneath the shoulder is further subjected to extrusion by the tool rotational and

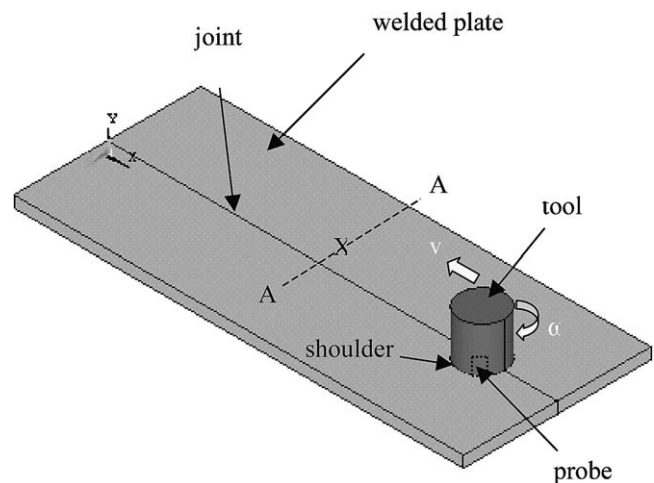


Fig. 1. A schematic illustration of FSW process.

* Corresponding author. Tel.: +1-214-768-4873; fax: +1-214-768-0812.

E-mail address: kovacevi@seas.smu.edu (R. Kovacevic).

transverse movements. It is expected that this process will inherently produce a weld with less residual stress and distortion as compared to the fusion welding methods, since no melting of the material occurs during the welding.

Despite significant advances in the application of FSW as a relatively new welding technique for welding aluminum alloys, the fundamental knowledge of such thermal impact and thermomechanical processes are still not completely understood. It is well known that the residual stress of the weld negatively affects its fatigue properties and its anticorrosion performance [2,3]. Several investigations of the residual stress distribution in FSW weld were conducted by experimental methods. Webster [4] reported a measurement of residual stress in FSW welded Al 7108 by the synchrotron X-ray technique, which shows that the longitudinal residual stress varies in the range from -60 to 140 MPa, and also shows a correlation between the detailed residual stress features and the heat flow in the weld. Sutton [5] investigated the residual stress in 2024-T3 aluminum friction stir butt welds using the neutron diffraction technique, and the results show that the highest stresses occur near the crown side of the weld over the entire FSW region. To gain physical insight of the FSW process and the evolution of the residual stress, the development of models and simulation techniques is a necessity. It will also be beneficial to use models and simulation techniques to minimize the residual stresses in the weld since this method will guide the implementation of the process with optimal parameters and with a minimum amount of trial-and-error.

Song and Kovacevic have modeled the heat transfer in FSW using the finite difference method [6,7]. Few papers have directly dealt with the modeling of the thermomechanical stresses in FSW. Chao [8] proposed a model to predict the thermal history and the subsequent thermal stress and distortion of the workpiece without involving the mechanical effect of the tool. Dong [9] developed several models to separately deal with the subproblems of heat transfer, material flow, and plastic flow. From the point of physics for the FSW process, the mechanical effect of the tool needs to be included into the thermomechanical model.

In this paper, a three-dimensional model based on a finite element method (FEM) is proposed to study the thermal impact and evolution of the stresses in the weld by considering the mechanical effect of the tool (only the shoulder is included at this time). This study is accomplished by parametrically studying the effects of varying welding parameters, primarily the traverse speed of the tool. The entire welding process is simulated using the commercial finite element package ANSYS. Experiments on a welding of Al 6061-T6 are also carried out. The temperature history and the in-plane biaxial residual stress for the welded plates are measured by the X-ray

diffraction (XRD) technique for a comparison with the calculated results.

2. Model description

The welding process is shown in Fig. 1, where V is the traverse speed of the tool, and ω is its rotational speed. The tool is made of AIRKOOL steel, and consists of the shoulder and probe, with the diameters of $R_0 = 24$ mm and $r_0 = 6$ mm, respectively. The welded plates are 6061-T6 Al alloy, each is in a rectangular shape with a size of $240 \times 50 \times 6$ mm. The tool is considered a rigid solid, and the workpiece is considered a ductile material characterized with elasticity, plasticity, and a kinetic hardening effect. The temperature-dependent properties of the 6061 Al alloy are used up to 371 °C based on Ref. [10]. For temperatures higher than 371 °C, the temperature-dependent properties of this aluminum alloy are extrapolated. The stress–strain curves of 6061-T6 at various temperatures are plotted in Fig. 2 [8].

2.1. Heat transfer model

The temperature calculation is based on Fourier's equation:

$$\rho c \frac{dT}{dt} = \text{div}(\kappa \cdot \text{grad}T) + q \text{ in } \Omega \quad (1)$$

where q is the power generated by friction between the tool and the top of the workpiece and by the plastic deformation work of the central weld zone, T is the temperature, κ is the conductivity, ρ is the material density, and c is the heat capacity.

The main heat source in FSW is generally considered to be the friction between the rotating tool and the welded plates, and the “cold work” in the plastic deformation of material in the vicinity of the tool. Considering an element at the contact surface between the tool shoulder and the top surface of workpiece, the rate of heat generation derived from the friction in the element at radius r is:

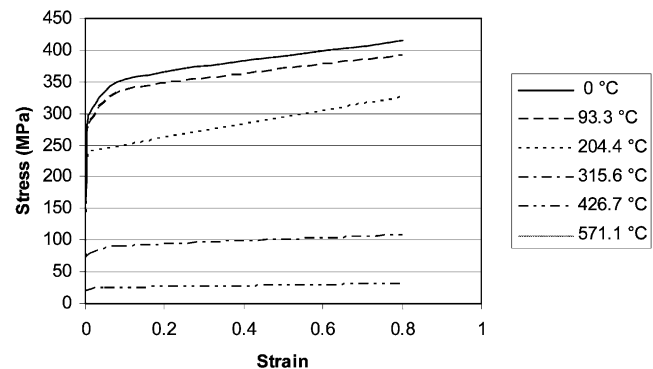


Fig. 2. Stress–strain curves of 6061-T6 used in the model.

$$d\dot{q} = 2\pi\omega \cdot r^2 \mu(T)p(T)dr \quad (2)$$

The rate of heat generation (caused by the friction) over the entire interface of the contact will be:

$$\dot{q} = \int_{r_0}^{R_0} 2\pi\omega \cdot r^2 \mu(T)p(T)dr = \frac{2}{3}\pi\omega\mu(T)p(T)(R_0^3 - r_0^3) \quad (3)$$

The rate of heat generation at the interface between the shoulder and the top of the workpiece surface is a function of the coefficient of friction μ , angular velocity ω , and radius r . As the $\mu(T)$ and $p(T)$ are dependent on the local temperature and the radius r , Eq. (3) is difficult to evaluate. As the temperature increases, the friction coefficient is expected to decrease, and the work of the plastic formation increases. In this model, the p is from the experimental measurement. A constant value of the friction coefficient is used to approximate the comprehensive effect of both factors of thermal and plastic effects during FSW, and the predicted temperature history is verified by the measured ones. The heat generation in the vicinity of the probe is considered the same as that at the shoulder periphery with a radius equal to that of the probe.

2.2. Mechanical model

The force equilibrium on an arbitrary volume results in the following governing equation known as the equilibrium equation:

$$\text{Div}(S) + F = \rho \cdot \gamma \quad (4)$$

where S is the stress tensor, ρ is the equivalent density, γ is the acceleration, and F is the volume force intensity. The inertial effect is neglected in this model since a constant rotational speed and a constant longitudinal speed are used during FSW.

In the displacement formulation, the essential boundary conditions are specified as

$$U = 0 \quad (5)$$

for the clamped portion of the plate surface and the normal displacement

$$U_y = 0 \quad (6)$$

for the bottom of the plate at $y = 0$.

2.3. Finite element model

The ANSYS as a commercial FEM software is used to carry out the numerical simulation. In the simulation, the thermomechanically coupled three-dimensional Lagrangian finite element model incorporating temperature and multilinear strain hardening effects is used for the three-dimensional modeling of the solid structures. The element topology used is eight nodes and has plasticity,

stress stiffening, large deflection, and large strain capabilities [11].

Symmetry along the weld line is assumed in the calculation, so one half of the welded plate is meshed with a total of 3537 nodes. In modeling the temperature history, the moving heat sources of the shoulder and the probe are represented as moving the heat generation of the nodes in each computational time step. The mechanical effect by the shoulder is involved in the mechanical model, as the relatively larger contact region of the shoulder and the workpiece is expected to contribute a large part of the mechanical stress, especially in the up-half part of the weld.

The temperature gradient is large around the welding zone and seriously changes the materials properties. In order to increase the accuracy of the mechanical solution, the thermal and mechanical solutions are coupled: the temperature data at each increment time is used to evaluate the mechanical properties and the thermal parameters.

3. Experiment setup

3.1. FSW implementation

Two 6060-T6 Al alloy plates, each with a dimension of $240 \times 50 \times 6$ mm are butt welded in the adapted vertical milling machine for FSW. In the experiments, eight thermal couples are embedded in one plate of which four are located 1.6 mm below the top surface and the other four are located 1.6 mm from the bottom surface, with a distance of 10, 14, 22, and 30 mm, respectively, to the weld centerline. The space of the thermocouples in the longitudinal direction is 10 mm. A sensor based on a micrometer measurement unit is used to monitor the plunge depth of the tool. Temperatures are acquired and recorded in a time-duration of 0.1 s by a Labview-programmed acquisition system. The specimens, each having dimensions of 29×29 mm are cut with a waterjet cutting machine and are subsequently polished. At least 0.02 mm depth of the outer layer of the specimen was etched away with Keller's reagent to minimize the mechanical effect induced by the sample polishing.

3.2. X-ray residual stress measurement

A Sintag (Thermo ARL) PAD V Powder X-ray diffraction (XRD) system, which is configured with a vertical 2-Theta:Theta X-ray goniometer, high intensity Cu X-ray tube, and a Kevex psi peltier cooled silicon detector is used for residual stress measurement. The standard quartz is used for the calibration. Automation and data collection is accomplished through a personal computer

running Windows NT and the latest version of Scintag's DMSNT software including stress analysis.

The principle of stress analysis by XRD is based on measuring the angular lattice strain distributions. That is, we choose a reflection at high 2θ and measure the change in the d -spacing with different orientations of the sample top surface (x - z plane). Using Hooke's law, the stress can then be calculated from the strain distribution. The aluminum (422) reflection is used to determine the strain. The strain distribution is measured by determining the d -space, $d_{\phi,\psi}$, at various tilt angle (ψ) of the sample. In terms of the angles ϕ and ψ , the strain can be expressed as:

$$\varepsilon_{\phi,\psi} = \frac{d_{\phi,\psi} - d_0}{d_0} = \frac{1 + \nu}{E} S_{\phi} \sin^2 \psi - \frac{\gamma}{E} (S_{xx} + S_{zz}) \quad (7)$$

where E is Young's modulus of elasticity, γ is Poisson's ratio, d_0 is the lattice spacing in the unstressed state.

The stress component along the ϕ -direction is given by:

$$S_{\phi} = S_{xx} \cos^2 \phi + S_{xz} \sin(2\phi) + S_{zz} \sin^2 \phi \quad (8)$$

The biaxial surface stresses are calculated using the Eqs. (7) and (8), and determined directly from the slope of a least-squares of d versus $\sin^2(\psi)$.

4. Results and discussion

4.1. Typical microstructure of the FSW weld

The microstructure of the weld is resulted from a dynamics of the physical process and is strongly relevant to the thermal history and/or the plastic deformation of the weld region, and it also affects the residual stress distribution. Fig. 3 shows a typical optical micrograph taken from the metallographically prepared specimen. The micrograph reveals four distinct regions: (a) stirred weld zone (or weld nugget); (b) thermomechanically affected zone (TMAZ); (c) heat affected zone (HAZ); and (d) base metal. In the nugget region, the refined grains are equiaxed and are attributed to the dynamic recrystallization as a result of the heat and mechanical work. The HAZ usually contains a large amount of

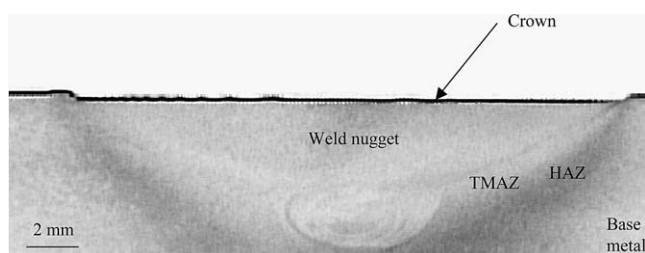


Fig. 3. Typical microstructure of the weld in the cross-section perpendicular to the welding direction.

coarsened grains with relatively lower yield strength than that in the TMAZ and the nugget, which is believed to be the weakest place for the crack initiation in the tests of fatigue performance and tensile strength.

4.2. Study of temperature–time history in FSW

Fig. 4 shows the temperature and temperature gradient contours in the cross-section perpendicular to the welding direction. The highest temperature is observed in the center of the weld region extending down from the crown surface to the probe root side, since the rotation of the shoulder and probe contributes the highest heat flux in this region. The relatively higher heat dissipation through the contact surface between the welded plate and the backing plate as compared with the top surface of the plate causes the temperature contour in the weld nugget area to follow a “V” shape. Fig. 4(b) shows that the maximum temperature gradient in the lateral direction (z -direction) happens in the region formed by the edge of the shoulder. This event is attributed to the fact that the highest heat generation in this region and the highest heat radiation dissipation of the region occur just beyond the shoulder edge. The temperature and temperature gradient contours in the longitudinal direction for the top surface during welding are revealed in Fig. 5, which proves that the region contacted with the periphery edge of the shoulder is subjected to the highest thermal impact effect. It is believed that the described “V”-type distribution of the temperature in the weld zone contributes to the grain coarsening in the TMAZ and the HAZ shown in Fig. 3.

Fig. 6(a) shows a comparison of the calculated and the measured temperature–time history at the location 10 mm to the weld centerline and 1.6 mm below the top surface of the plate. The rotational and the traverse speeds of the tool are 500 rpm and 140 mm/min, respectively. In the initial stage of the welding, the calculated values are higher than the measured ones, but they are less than the measured ones after the maximum tempera-

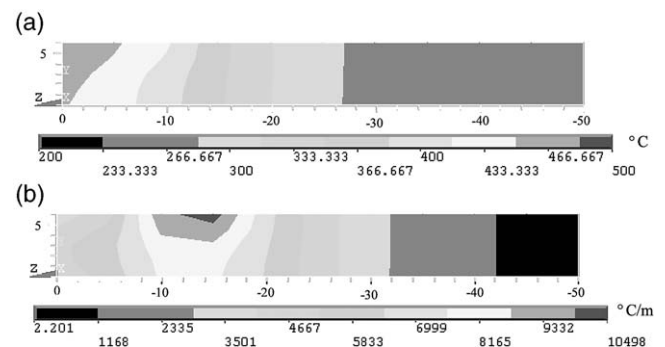


Fig. 4. (a) Temperature contour and (b) temperature gradient (z -direction) contour in the A–A cross-section perpendicular to the weld direction at the moment the tool moves to the middle point of the plate ($V = 140$ mm/min, $\omega = 500$ rpm).

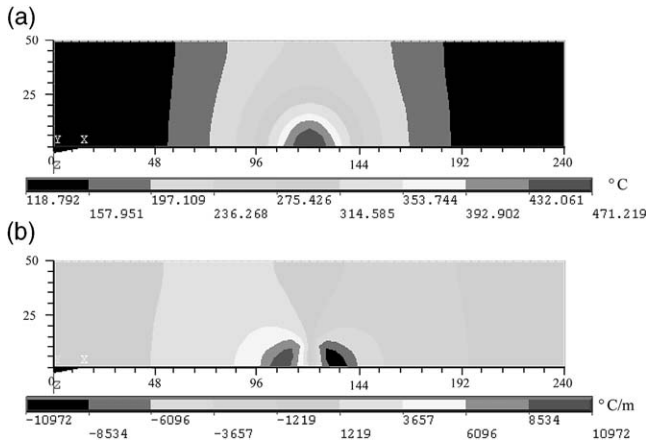


Fig. 5. (a) Temperature contour and (b) temperature gradient contour (x -direction) in the top surface of the welded plate at the moment the tool moves to the middle point of the plate ($V = 140$ mm/min, $\omega = 500$ rpm).

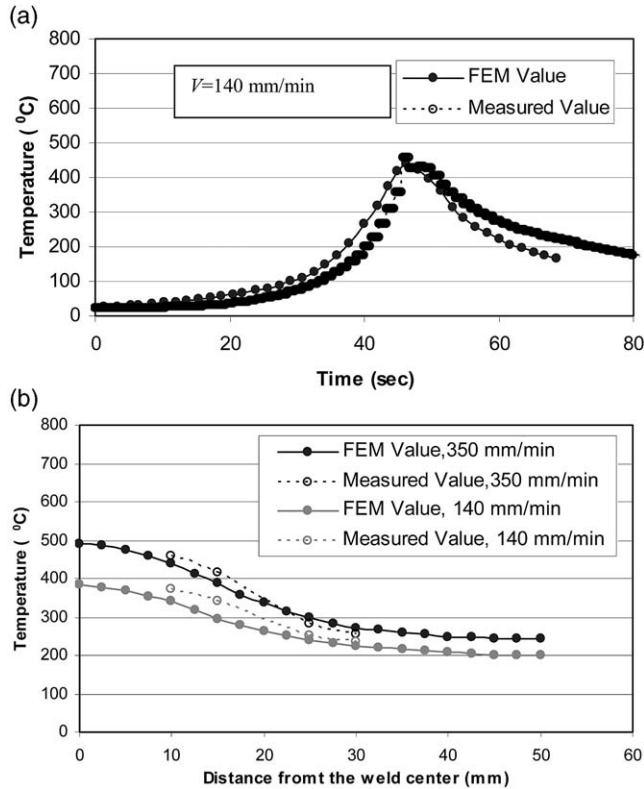


Fig. 6. A comparison of the calculated and the measured temperature history. (a) Temperature–time profile for the location 10 mm to the weld centerline and 1.6 mm below the top surface of the plate ($V = 140$ mm/min, $\omega = 500$ rpm), (b) temperature profile along the A–A direction.

ture is reached, which may be caused by the assumption of a constant temperature of the backing plate. Actually, the temperature of the backing plate rises because of the heat buildup during welding, which decreases the cooling rate of the weld in the later stage of welding. Nevertheless, the calculated temperature values in the entire

welding process are in a reasonable agreement with the measured ones. Fig. 6(b) shows a temperature distribution along the lateral direction (for nodes 1.6 mm below the top surface of the plate) at the instant when the shoulder's center is passing over this location by two traverse speeds of 140 and 350 mm/min, respectively. It is obvious that the increase of the traverse speed of the tool will significantly decrease the temperature of the welded plate, especially in the weld zone. A good agreement between the measured and calculated temperature indicates that the developed model for the prediction of temperature history is providing satisfactory results.

4.3. Analysis of stress distribution in the weld

The stress will form in the weld during welding since the expansion of material occurs during the heating of the welded plates, followed by the contraction during the cooling of the welds. Furthermore, the rotational and the transverse movements of the tool will cause additional stress in the weld due to the mechanical constraint of the plates by the fixture.

Fig. 7 shows the residual stress contours in three orthogonal directions of the welded plate. The longitudinal stress contour (Fig. 7(a)) and lateral stress (S_z) contour (Fig. 7(c)) show that the predicted maximum stress is located appropriately in the middle of the weld length. The predicted stress distribution in Fig. 7 is like the one encountered in steel welds [12], and also complies with measurements on friction stir welded Al 2024-T3 with the cut compliance method reported by Dalle Donne et al. [2]. It is noticed that the start-portion and end-portion of the weld have different stress distributions as compared with the mid-portion of the plate, which may be caused by the variance in the correlated thermomechanical process during the welding. The throughout-thickness stress, S_y (see Fig. 7(b)), reveals not much variation through the thickness. At the end-portion of the weld, the lift-up of the tool leaves the keyhole region in a compressive stress state as shown in Fig. 7.

Fig. 8 shows the residual stress distribution in the longitudinal direction (x -direction) and the lateral direction (z -direction) in the cross-section at the middle of the weld, with travel speeds of 140 and 350 mm/min, respectively. The longitudinal stress (Fig. 8(ia), (iia)) reveals maximum value in the region extending down from the crown surface in a depth of 1.5 mm for 140 mm/min and 3.5 mm for 350 mm/min in the weld nugget, and tapers throughout the thickness to the bottom surface of the plate. In the top-half of the weld region, S_x and S_z are in tensile stresses, and taper significantly beyond the edge of the shoulder along the lateral direction. These simulated results comply with the stain maps of the friction stir weld with the synchrotron XRD technique [4]. It is also noticeable that the higher tool traverse speed results in a larger high longitudinal stress

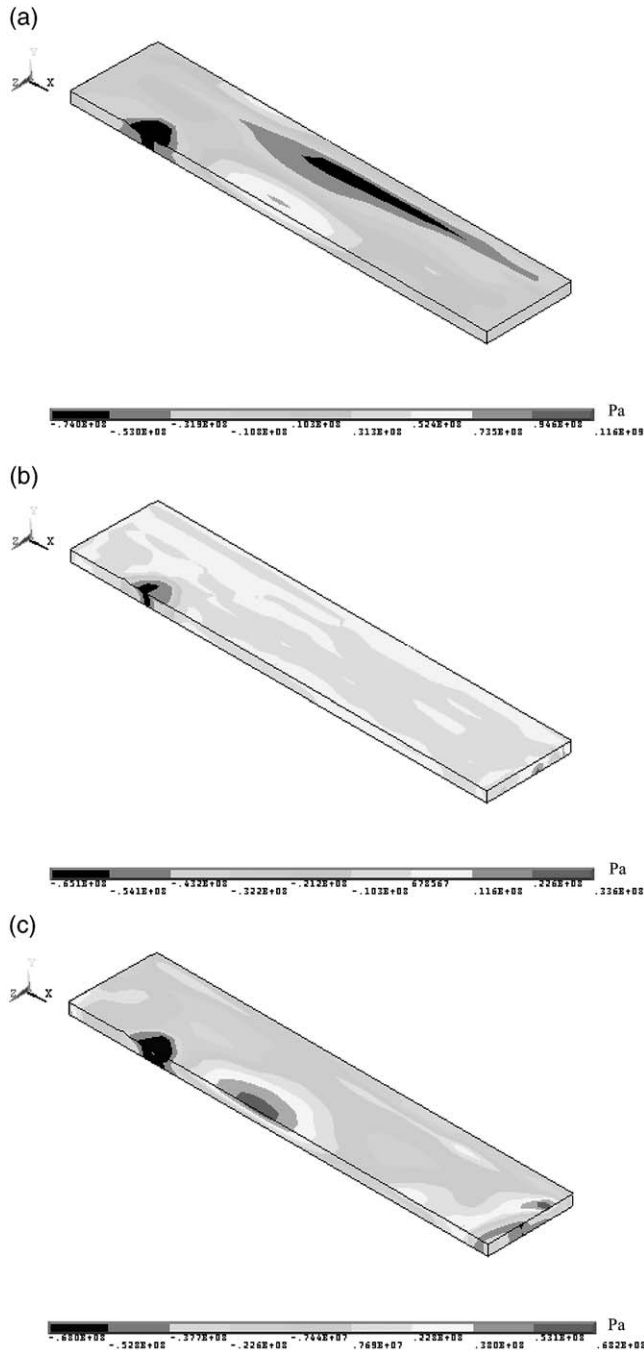


Fig. 7. Predicted three-dimensional residual stress distribution in the welded plate. (a) x -direction, (b) y -direction, and (c) z -direction ($V = 140$ mm/min, $\omega = 500$ rpm).

region (Fig. 8(ia), (iia)) and a narrower higher lateral stress region (Fig. 8(ib), (iib)) extending down from the crown surface.

Fig. 9 shows the three orthogonal stress distributions along the line A–A (as indicated in Figs. 1 and 8) on the top surface of the plate. Before the fixture is released, the lateral stress (maximum value 316 MPa) reveals higher values than the longitudinal stress (maximum value 139 MPa), both of which reveal tensile values. After the fix-

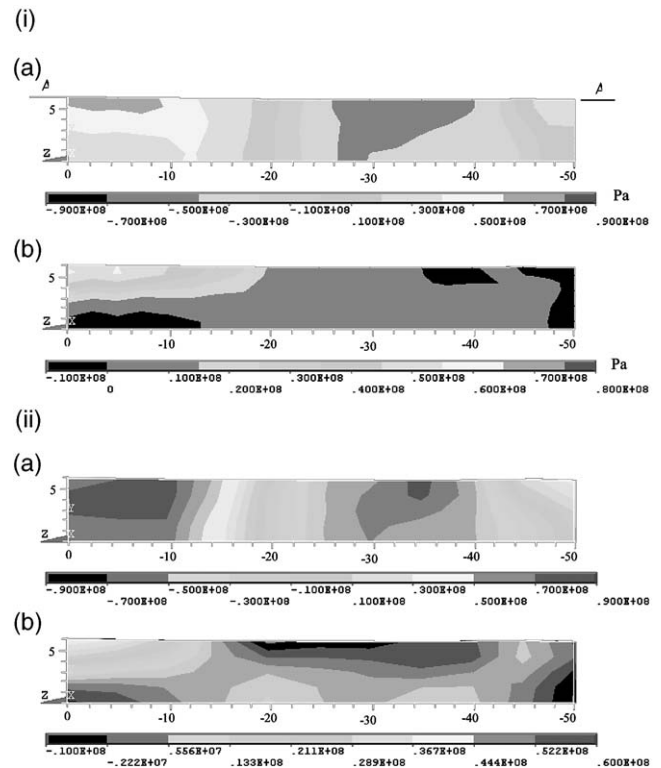


Fig. 8. Predicted residual stress contour of (a) S_x and (b) S_z in the A–A cross-section perpendicular to the weld direction. (i) $V = 140$ mm/min, (ii) $V = 350$ mm/min.

ture is released, both S_x (maximum value 74.3 MPa) and S_z (maximum value 50 MPa) decrease significantly, and S_x reveals higher values than S_z along the lateral direction to not far beyond the edge of the shoulder, as shown in Fig. 8(b). In the range between 20 and 45 mm from the centerline, the longitudinal stress reveals compressive values. Similar residual stress distribution was observed in the friction stir welded aluminum of 7xxx series alloys [13]. Fig. 9c also shows that the higher traverse speed induces an increase in the longitudinal stress from 74.3 to 87 MPa, and a decrease in the lateral stress from 50 to 42 MPa. A similar observation for the residual stress measurement of 6061-T6 Al alloy by neutron diffraction was also reported by Wang et al. [14]. The measured residual stress values are also plotted in Fig. 9(b) and (c). Although some deviations exist between the predicted values and the measured ones, the distribution of the predicted residual stress reveals a reasonable agreement with the measured one. The vertical residual stress (S_y) along the line A–A is predicted in a range of -1.7 to 8.3 MPa, much lower than the lateral and the longitudinal stresses, and is negligible in evaluating the in-plane stress at the top surface of the plate with the XRD technique.

From the above description, it is clear that the locations of the high gradient in the residual stresses in both the longitudinal and the lateral directions are in the

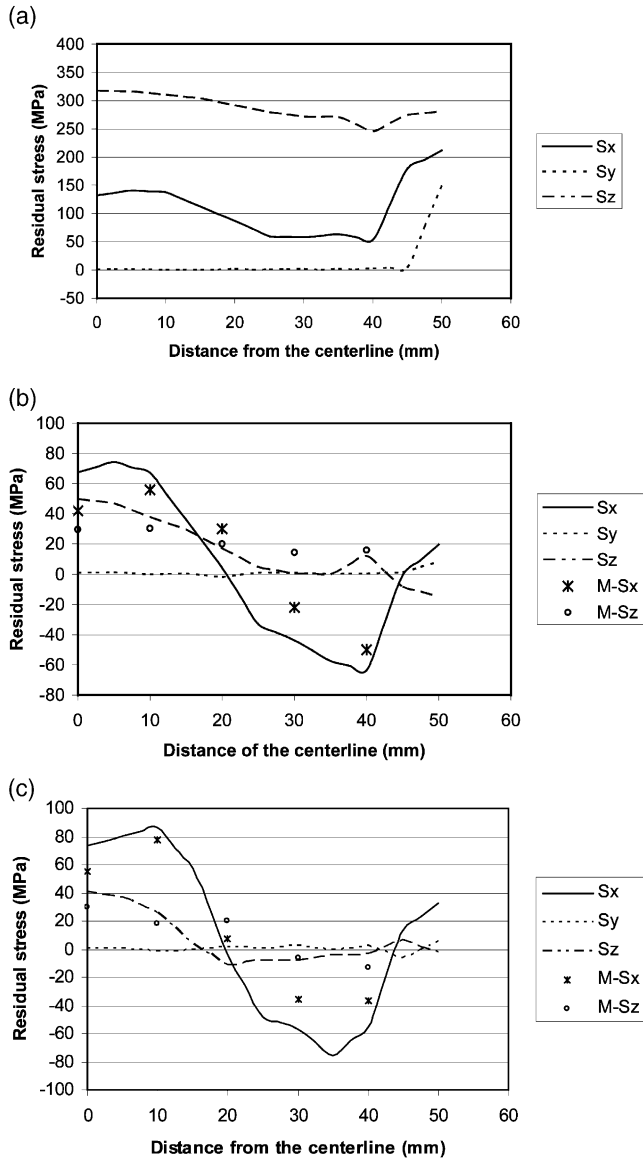


Fig. 9. Predicted stress (S_x , S_y , S_z) distribution and measured stress values (M- S_x , M- S_y) along the line A-A in the top surface of the plate as shown in Fig. 1; (a) After welding and before the fixture release, $V = 140$ mm/min; (b) after fixture release, $V = 140$ mm/min; (c) after fixture release, $V = 350$ mm/min.

proximity of the shoulder diameter (12 mm from the centerline), which is believed to be caused by the high temperature gradient (see Figs. 4(b) and 5(b)) and high shear force by the shoulder periphery edge in this region. The sharp changes of temperature and down force at the edge of the shoulder also contribute to the sharp gradient in microstructure as observed in Fig. 3. The higher tool traverse speed will induce a lower heat input to the weld zone, and will result in a greater high-stress zone with a higher stress value in the weld, because the relatively harder metal in the weld zone causes a greater resistance to the plastic extrusion.

In order to provide a quantitative framework for

understanding the dynamics of the thermomechanical process of FSW, the predicted nodal stress evolution for the node located at the X position (10 mm from the centerline, shown in Fig. 1) is plotted in Fig. 10. It is revealed that the compressive stresses are formed in both the longitudinal and the lateral directions in front of the tool, and decrease with the tool moving near to the node position. It is interesting to note that S_x changes from compressive values to tensile values (maximum of 25.3 MPa) when the tool moves to appropriate 15–4 mm behind the node location, and then changes again to compressive values (maximum of 33.4 MPa) again appropriately 20 mm in front of the node location. Similarly, S_z changes from compressive values to tensile values (maximum of 8 MPa) when the tool moves to appropriately 11–6 mm behind the node location, then changes again to compressive values (maximum of 55.4 MPa) appropriately 14 mm in front of the node location.

The vertical stress-component S_z reveals tensile values until the tool moves near the node location, over which it shows compressive values. Obviously, when the tool moves to a specific range of distance from the node location (appropriately from 11 to 6 mm in this case), all three stress-components reveal tensile values, and it is speculated that the most likely welding defects will occur in this region.

Fig. 10 also shows that the lateral stress S_z is generally larger than the longitudinal stress S_x during the welding before the fixture is released. In the later welding stage after the tool travels over the node location, the lateral stress for the node X reveals tensile values and increases with the time before the fixture is released, because the increased contraction of the weld as a result of the cooling is restrained by the fixture. A release of the fixturing induces a significant decrease of both the lateral and longitudinal stresses, with S_z less than S_x . From this point, controlling the fixturing condition during the welding and the post-welding can be employed to control the residual stresses and deformation, and to prevent

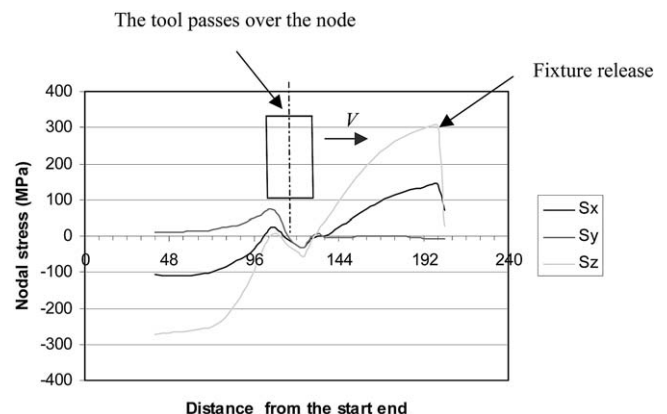


Fig. 10. Predicted nodal stress (S_x , S_y , S_z) evolution for X position (10 mm from the centerline) during the FSW, $V = 140$ mm/min.

cracking in the weld. It is also noted that the through-thickness stress, S_y , reveals an increasing trend until the tool traverses to the node location, where it decreases in magnitude to a negligible value.

5. Conclusions

A three-dimensional thermomechanical model including the mechanical action of the shoulder and the thermomechanical effect of the welded material is developed for the FSW of an Al-alloy, in order to build qualitative framework to understand the thermomechanical process in FSW. Modeling and measurement of the temperature and stress evolution in the FSW of 6061-T6 Al alloy is conducted, and the experimental values validate the efficiency of the proposed model.

The prediction and measurement show that the maximum temperature gradients in longitudinal and lateral directions are located just beyond the shoulder edge, and also show that the longitudinal residual stress is greater than the lateral residual stress at the top surface of the weld. The prediction shows that the high stress is located in the region extending down from the crown to the mid-thickness of the weld. A higher traverse speed induces a larger high longitudinal stress zone and a narrower lateral stress zone in the weld, which complies with the previously reported measurements with the synchrotron and neutron techniques. Moreover, the prediction reveals that the fixturing release to the welded plates will affect the stress distribution of the weld. Further development of the FSW requires assessment of the mechanical action of the probe and the fixturing condition to the stress distribution of the welded plates.

Acknowledgments

This work has been financial supported by the US Department of Education, grant no. P200A80806-98, Brown Foundation, Houston, TX, and SMUs Research Center for Advanced Manufacturing, Richardson, TX. Assistance by Michael Valant, research engineer, during the experiments is gratefully acknowledged.

References

- [1] W.M. Thomas, E.D. Nicholas, J.C. Needham, M.G. Murch, P. Templesmith, C.J. Dawes, "Friction stir butt welding" International patent application no. PCT/GB92/02203 and GB patent application no. 9125978.8, 6 December 1991.
- [2] C. Dalle Donne, G. Biallas, T. Ghidini, G. Raimbeaux, Effect of welding imperfections and residual stresses on the fatigue crack propagation in friction stir welded joints, in: Second International Symposium on Friction Stir Welding, Gothenburg, Sweden, 26–28 June, 2000.
- [3] F. Zucchi, G. Trabanelli, V. Grassi, Pitting and stress corrosion cracking resistance of friction stir welded AA 5083, *Materials Corrosion* 52 (11) (2001) 853–859.
- [4] P.J. Webster, L. Djapic Oosterkamp, P.A. Browne, D.J. Hughes, W.P. Kang, P.J. Withers, G.B.M. Vaughan, Synchrotron X-ray residual strain scanning of a friction stir weld, *Journal of Strain Analysis* 36 (1) (2000) 61–70.
- [5] M.A. Sutton, A.P. Reynolds, D.Q. Wang, C.R. Hubbard, A study of residual stresses and microstructure in 2024-T3 aluminum friction stir butt welds, *Journal of Engineering Materials and Technology ASME* 124 (4) (2002) 215–221.
- [6] M Song, R. Kovacevic, Thermal modeling of friction stir welding in a moving coordinate and its validation, *International Journal of Machine Tool and Manufacturing* 43 (6) (2003) 605–615.
- [7] M Song, R. Kovacevic, Numerical simulation and experimental analysis of heat transfer process in friction stir welding process, *Proceeding of Institution of Mechanical Engineers, Part B, Journal of Engineering Manufacture* 216 (12) (2002) 73–85.
- [8] Y. Cao, X. Qi, Thermal and thermo-mechanical modeling of friction stir welding of aluminum alloy 6001-T6, *Journal of Materials Processing and Manufacturing Science* 7 (10) (1998) 215–233.
- [9] P. Dong, F. Lu, J.K. Hong, Z. Cao, Coupled thermomechanical analysis of friction stir welding process using simplified models, *Science and Technology of Welding and Joining* 6 (5) (2001) 281–287.
- [10] Handbook of Aluminum, Alcan Aluminum Corporation, 1970.
- [11] AYSYS User's Manual: Elements, vol III, Swanson Analysis Systems, Inc.
- [12] K. Masubuchi, *Analysis of Welded Structures*, Pergamon Press, Oxford, NY, 1980.
- [13] L. Djapic Oosterkamp, P.J. Webster, P.A. Browne, G.B.M. Vaughan, P.J. Withers, Residual stress field in a friction stir welded aluminum extrusion, *Materials Science Forum* 247-349 (2000) 678–683.
- [14] X.L. Wang, Z. Feng, S.A. David, S. Spooner, C.R. Hubbard, Neutron diffraction study of residual stresses in friction stir welds, in: Proceedings of the ICRS 6 (Residual Stresses: International Conference on Residual Stresses), IOM Communications, London, UK, 2000, pp. 1408–1415.